Journal of the Korean Ceramic Society (2022) 59:859–868
https://doi.org/10.1007/s43207-022-00222-z

ORIGINAL ARTICLE

ZnO nanostructures for photocatalytic degradation of methylene blue: effect of different anodization parameters

Ahmet Emrecan Oksuz[1] · Metin Yurddaskal[2] · Ugur Kartal[3] · Tuncay Dikici[4,5] · Mustafa Erol[2,5]

Received: 18 February 2022 / Revised: 27 April 2022 / Accepted: 4 June 2022 / Published online: 18 July 2022

Abstract
In this paper, the photocatalytic activity of ZnO nanostructures formed by anodization method with different parameters was investigated. The synthesis of ZnO nanostructures with different morphology by varying anodic oxidation parameters containing electrolytes, molarity, voltage, and duration was analyzed. ZnO nanostructures were prepared through different parameters consisting of six samples. The produced ZnO nanostructures were investigated by using X-ray diffraction, scanning electron microscopy, diffuse reflectance spectroscopy, and UV–Vis spectrophotometer. It was found that the morphology of ZnO structures was formed as nanorods, needle-like, flower-like, heterogeneous, and homogeneous of mixed structures. ZnO nanostructures were identified by matching X-Ray diffraction peaks due to the international center for diffraction data database. Experiments on photocatalytic degradation of methylene blue demonstrated that the photocatalytic activity of ZnO samples. The best photocatalytic performance was observed by the sample anodized for an hour in 0.05 M of $KHCO_3$ electrolytes with 40 V electrical potential. It was observed that the removal of methylene blue increased 3 times (photocatalytic degradation efficiency ~ 31% for methylene blue vs ~ 90% by the best sample) thanks to the obtained ZnO nanostructured photocatalysts. The results showed that an increment of the voltage has a significant effect on the photocatalytic activity of ZnO while keeping other parameters including molarity, time, and electrolyte type constant.

Keywords ZnO nanostructures · Anodic oxidation · Photocatalytic activity · Cotton-like fiber ZnO

1 Introduction

Ecological pollution is one of the most important problems for the health of human beings, especially industrial facilities unload above 300 million tons of heavy metal, chemical wastes, and toxic wastes year after year [1]. These chemicals which are phenols, detergents, and synthetic dyes deliver to the wastewater stream [2]. To eliminate these pollutants, photocatalysis with solar irradiation is an encouraging approach. Semiconducting materials, such as TiO_2, ZnO, and SnO_2 have a great future as photocatalyst materials [3, 4]. Between these oxides, ZnO is an efficient semiconductor for photocatalytic application to compare with TiO_2, ZnO has higher electron mobility, has higher oxidation rate, and is cheaper [5]. ZnO is an inorganic composite composing of transitional element. Although the solubility of ZnO is limited in water it is great in acids and bases. ZnO has a large bandgap of 3.2 eV as a semiconductor, which is suitable for photocatalysis reaction beneath ultraviolet (UV) source [6]. The higher surface area/defects are essential physical factors to determine the photocatalytic action of oxides. In the current photo-degradation process, the transition metal oxides are utilized as catalysts [7].

Methylene blue (MB) is a very common dye that is widely used in many industries. Notwithstanding, their release into the ecosystem results in water pollution [8–10]. The degradation process of MB by photocatalysis depends on light-sensitive semiconductors, in a viable improving selection, has become a very favored field for

✉ Ugur Kartal
ugurkartal@iyte.edu.tr

1 The Graduate School of Natural and Sciences, Dokuz Eylul University, Izmir, Turkey

2 Department of Metallurgical and Materials Engineering, Dokuz Eylul University, Izmir, Turkey

3 Department of Materials Science and Engineering, Izmir Institute of Technology, Izmir, Turkey

4 Torbali Vocational School, Dokuz Eylul University, Izmir, Turkey

5 Center for Fabrication and Application of Electronic Materials, Dokuz Eylul University, Izmir, Turkey

wastewater treatment, especially when using a sustainable energy source because of their efficiency and lack of minor pollution [11–15].

In the photocatalytic process, the semiconductors go through photoexcitation by visible (Vis) or near infrared light. The sensing system of these semiconductors depends on the propagation of photo-induced electron/hole (e^-, h^+) couple upon irradiation by adequate light energy. These e^-–h^+ couple generate greatly reactive species, which then react with dye particles ravage their initial frame [16–20]. The most extensively used photocatalytic substance containing zinc oxide and titanium oxide are wide-bandgap semiconductors, which are incapable of absorbing visible lights directly [21–24]. Therefore, unchanged semiconductors are not convenient for the photocatalytic process. ZnO nanoparticles with different designs and features have drawn interest for photocatalytic operations in many fields such as nature and power areas. Up to the present, over 2500 papers have been pressed about the photocatalytic activity of ZnO nanoparticles. These researches studied the effect of different parameters, such as production technique, composition, and morphology.

There are many synthesizing methods for nanoscale ZnO including anodization [25–31], sol–gel method [32–34], template method [35–37], hydrothermal method [38–46], microwave irradiation [47, 48], and alkaline synthesis [49]. Among all these methods anodization is cheaper, environmentally friendly, and has a long-life span. Scientists reported that electrochemically synthesized ZnO has shown great photocatalytic activity on dye degradation [50, 51].

In this research, ZnO nanostructures have been grown by the anodization method. Different parameters were used to achieve the desired structure. Three different solutions for anodization were prepared. These solutions consisted of Potassium bicarbonate ($KHCO_3$), Sodium carbonate–Sodium bicarbonate (Na_2CO_3–$NaHCO_3$), and ethanol–sulfuric acid (C_2H_5OH–H_2SO_4). Produced ZnO structures were characterized by XRD, SEM, and UV–Vis spectrophotometer. The photocatalytic activity of ZnO structures was analyzed by using the methylene blue (MB) degradation as common dyes under UV–Vis light illumination.

2 Experimental details

2.1 Materials

Bulk zinc (99% purity) was purchased from the metal industry. $KHCO_3$ (99.7%), absolute C_2H_5OH (≥ 99.9), acetone (C_3H_6O, 99.9%), H_2SO_4 (95–97%), Na_2CO_3 (≥ 99.9%), and $NaHCO_3$ (≥ 99%) were supplied by Merck.

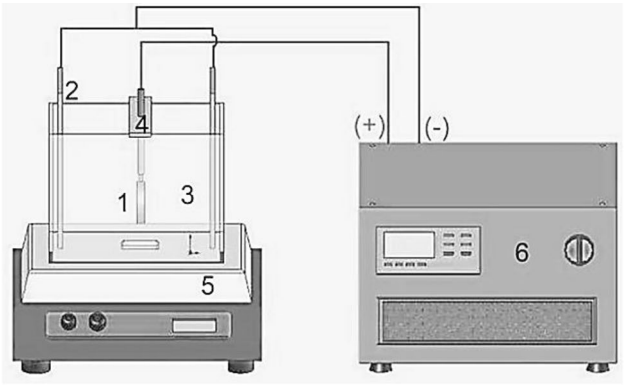

Fig. 1 Schematic diagram of the electrochemical anodic oxidation (1) anode (2) cathode (3) electrolyte (4) anode holder (5) hot plate (6) power supply

Table 1 Parameters of anodic oxidation process

Sample code	Solution (in H_2O)	Voltage	Duration (min)
S1	0.05 M $KHCO_3$	20	30
S2	0.05 M $KHCO_3$	20	60
S3	0.05 M $KHCO_3$	40	30
S4	0.05 M $KHCO_3$	40	60
S5	100 ml C_2H_5OH–0.2 M H_2SO_4	40	60
S6	Na_2CO_3–$NaHCO_3$ (0.6–0.6 g/L)	40	60

2.2 Synthesis of ZnO nanostructures

Before anodization, a large portion of bulk Zn was cut off into 6 pieces with dimensions 3 × 3 cm^2. These samples were sanded up to #180, #250, and #400 (# refers to grit number of the final sandpaper used and sample code designation using SiC emery papers (EAC-SiC supraflex paper). Samples were then sonicated in C_2H_5OH, C_3H_6O, and deionized water in an ultrasonic bath for 10 min separately. The anodic oxidation experiments were executed using a scheme (Fig. 1) including sanded zinc plates, platinum electrode, and various solutions as the anode, cathode and electrolyte, respectively. The distance between the electrodes was 15 cm. The anodic oxidation process was performed according to anodization parameters (Table 1) at room temperature. Produced ZnO samples were heat-treated at 300 °C for 1 h with a heating rate of 5 °C/min. The active surface area of electrodes was kept at 9 cm^2 for the purpose of electrochemical anodization.

2.3 Materials characterization

The crystallographic structure of the samples was examined by an X-ray diffractometer (Thermo Scientific ARL X'TRA, XRD) with a Cu-K_α (1.54185 Å) irradiation. Diffraction patterns were collected at the scan rate of 2°/min in the 2θ range 5°–90° at room temperature. Scanning electron microscopy (SEM, Carl Zeiss 300VP) was operated to monitor the morphology and microstructure of the samples. The optical properties of ZnO NWs were investigated with diffuse reflectance spectroscopy (DRS, Thermo Scientific Evolution600).

2.4 Photocatalytic measurements

10^{-5} M (3.2 mg/L) MB dye was arranged to observe the photocatalytic performance of the ZnO nanostructures. The photocatalytic degradation of MB was studied under a UV–Vis light source which was 300 W Osram Ultra-Vitalux E27 (4.3% UVA, 1% UVB, 94.47% Vis). ZnO nanostructures which were considered as a catalyst were put into beakers that contained 40 ml of MB dye with the help of a tweezer. Additionally, a catalyst-free sample was investigated to contrast with the outcome acquired from catalyzed samples. The distance between the UV–Vis light source and beakers was kept as 20 cm for all samples to adjust the light intensity to 0.55 W/cm^2. The reduction of absorbance intensity of the MB dye was observed utilizing the UV–Vis spectrophotometer (Shimadzu UV 1240 spectrophotometer) at 664 nm which matches the characteristic peak of MB [52]. In the experiment, 3 ml of liquid from the beakers was extracted transitorily at 60th, 180th, 270th, 390th, 510th, 630th, and 750th min. The observed absorbance values were transformed to concentration values usage utilizing Beer–Lambert's law interrelationship obtained in our former publication [53, 54]. The degradation efficiency of ZnO nanostructures were determined based on the formula $[(C_0 - C)/C_0] \times 100$ (C_0 initial concentration, C final concentration).

3 Results and discussions

3.1 Structural analysis

In the XRD pattern of the produced ZnO samples on the Zn plates shown in Fig. 2, it can be said that the produced ZnO nanostructures show strong, sharp, and intense diffraction peaks. Having strong, sharp and intense diffraction peaks is an indication of the presence of highly crystalline phases, which means the increased crystallinity of the fabricated ZnO nanostructures. XRD peak intensities differ from each other in terms of surface morphologies and oxide layer thicknesses, which vary due to different anodizing parameters. The peaks were observed at 31°, 34°, 36°, 47°, 56° and 63° belonging to the (100), (002), (101), (102), (110) and (103) planes of polycrystalline ZnO [55]. It has been observed that peaks in all produced films belong to the hexagonal wurtzite structure of ZnO (ICDD 36-1451) [56]. In addition, peaks of the zinc substrate were observed in the XRD patterns of some samples. These peaks corresponding to the hexagonal structure of the Zinc metal with ICDD card numbers 87-0713 [57]. Based on the diffraction spectrum of the ZnO nanostructures prepared in Fig. 2, it is worth noting that there is no notable change in the produced ZnO nanostructures when the anodizing parameters are changed. XRD patterns of all produced anodic films are in general agreement with the results obtained previously by some researchers [58–60].

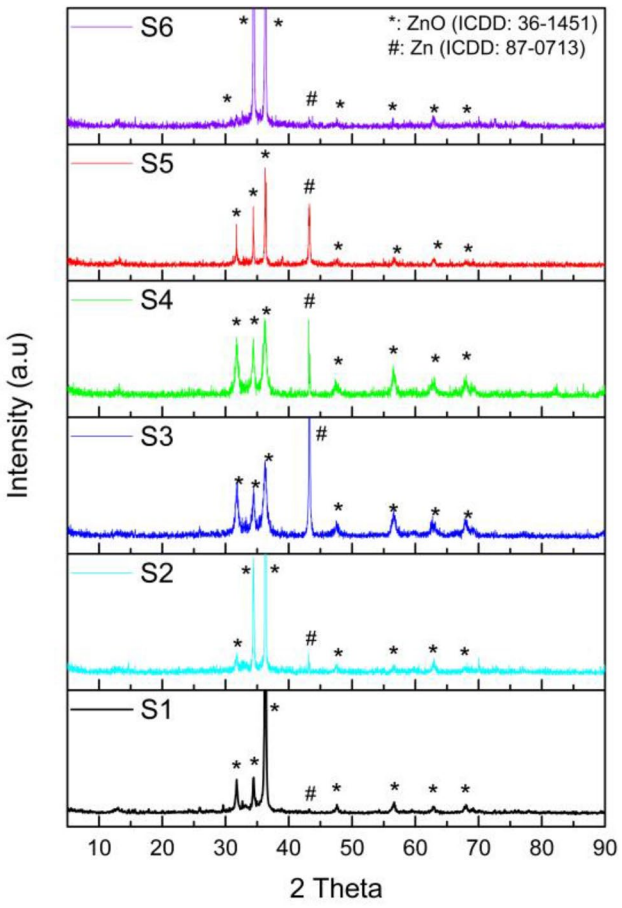

Fig. 2 XRD patterns of the ZnO nanostructures produced with different parameters

3.2 Morphological analysis

In the first step of electrochemical anodization, Zn^{2+} ions are originated from zinc foil owing to dissolution forming minor

and separated pits over its surface. The reason for the observation of the maximum current value is the low resistance value of the zinc foil and the current decreases rapidly due to the oxide layer formation. When monitoring via SEM, due to the high concentration of Zn^{2+} ions, nanostructures grow near or within the small holes of the surface. The reaction mechanism of nanostructures is as follows:

$$\text{At anode}: \quad Zn \rightarrow Zn^{2+} + 2e^{-}$$
$$Zn^{2+} + 2OH^{-} \rightarrow Zn(OH)_2$$
$$Zn(OH)_2 \rightarrow ZnO + H_2O$$
$$\text{At cathode}: \quad 2H^{+} + 2e^{-} \rightarrow H_2$$
$$\text{Dissolution}: \quad ZnO + HA \rightarrow ZnA + H_2O$$

where '*A*' refers to the HCO_3^- ions from the bicarbonate solution in the dissolution process.

ZnO nanostructures were grown by the anodization method is shown in Fig. 3. According to Fig. 3a, the needle-like ZnO nanostructures were performed in 0.05 M $KHCO_3$ solution at 20 V for 30 min. When the detailed inset picture

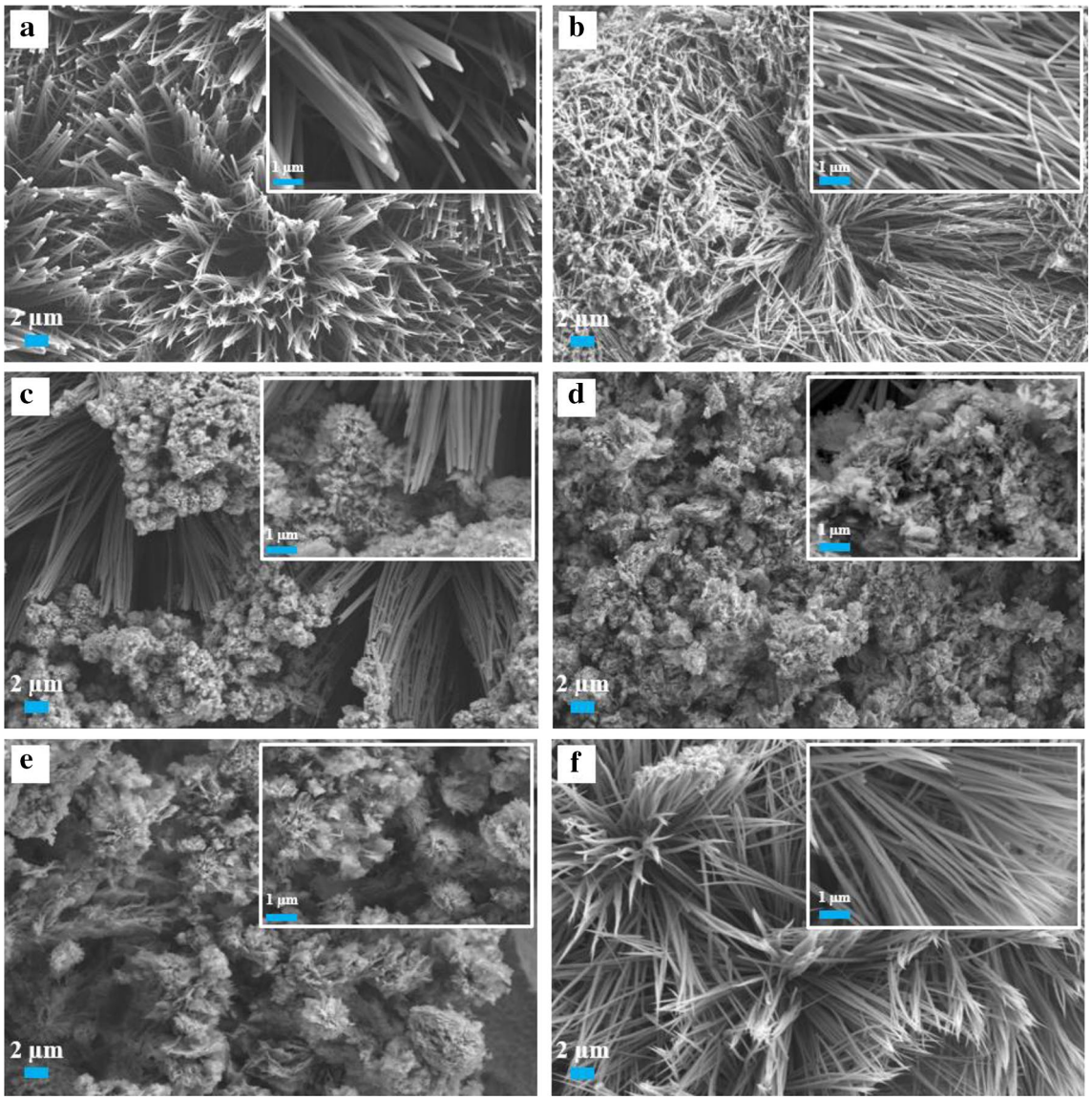

Fig. 3 SEM micrographs of zinc substrates anodized **a** in 0.05 M $KHCO_3$ solution at 20 V for 30 min, **b** in 0.05 M $KHCO_3$ solution at 20 V for 60 min, **c** 0.05 M $KHCO_3$ solution at 40 V for 30 min, **d** in 0.05 M $KHCO_3$ solution at 40 V for 60 min, **e** 100 ml C_2H_5OH and 0.2 M H_2SO_4 solution at 40 V for 60 min, **f** Na_2CO_3–$NaHCO_3$ (0.6–0.6 g/L) solution at 40 V for 60 min

is examined, we can state that these needle-like ZnO nanostructures cluster together and their approximate diameter is 250 nm. Figure 3b shows the ZnO nanowires which are produced in 0.05 M $KHCO_3$ solution at 20 V for 60 min by anodizing. It was observed that nanotube-like ZnO structures consisting of a dense and non-unidirectional alignment were formed with a 200 nm diameter. The samples whose morphologies are given in Fig. 3c and d were exposed to the same solution and voltage at different times. As a result of the anodizing process performed at 20 V, locally coexisting nanorods were observed, while the other high voltage (40 V) anodizing process has a more uniform structure. It can be seen from Fig. 3d, fine cotton-like fiber structures with very small diameters were obtained on the surface of S4. In this case, we concluded that the surface area increases significantly. Since the structures produced at 40 V and 60 min seem to be quite uniform, new nano-structures were produced with different electrolytes at these parameters. In Fig. 3e, we observed that a different structure from other morphologies. Dense and small-scale ZnO morphology was grown in 100 ml C_2H_5OH–0.2 M H_2SO_4 solution. The surface morphology with dense needle-like ZnO was obtained by the anodization of Zn substrate in Na_2CO_3–$NaHCO_3$ (0.6–0.6 g/L) solution (Fig. 3f).

As a result, as the dissolution rate increases with increasing electron density, selective corrosion in high-energy sites also accelerates. At the same time, since the number of ions in the anodizing bath also affects the anodizing process, different solutions cause variations in the obtained structure. For this reason, the structures with different morphology have been observed depending on the equilibrium between oxidation and dissolution with changing parameters.

The oxide layer thicknesses of the samples were measured with the help of the ImageJ program using SEM images and the obtained values were presented in Fig. 4. According to these results, the film thicknesses formed vary between 7.97 ± 0.48 and 17.26 ± 3.04 µm. This change in the oxide layer thickness, which has a significant effect on the photocatalytic activity, is due to the difference in the anodizing parameters.

3.3 Optical properties

DRS was used to obtain the wavelength versus reflectance data of the samples and the results are shown in Fig. 5. Using the reflectance data and the Kubelka–Munk function ($(F(R)h\upsilon)^n$), the bandgap was calculated. In the Kubelka–Munk function; hυ is the photon energy; R is the intensity of reflection; n is the value of the exponent indicated the character of the electronic transition, whether direct or indirect. n is ½ for direct bandgap materials, 2 for indirect bandgap materials. ZnO is well known to have a direct bandgap, therefore, $n = ½$ was selected [61]. The graph of the obtained $(F(R)h\upsilon)^{½}$ versus energy (eV) is

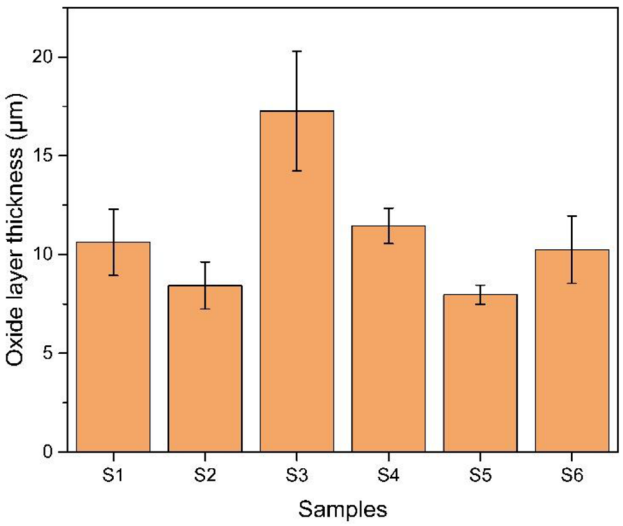

Fig.4 Oxide layer thickness of the samples

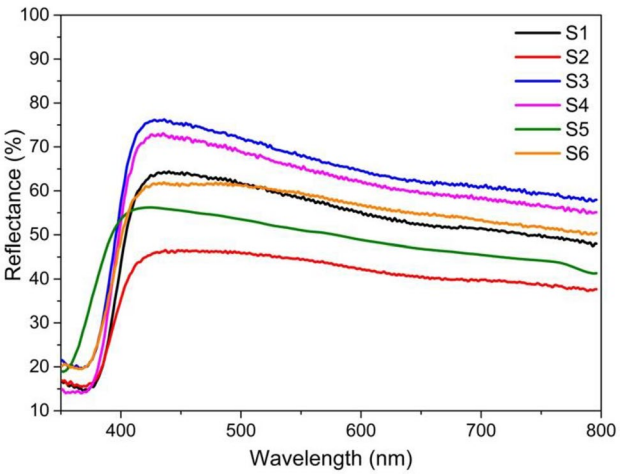

Fig. 5 Diffuse reflectance spectra of ZnO samples

shown in Fig. 6. The bandgap values obtained are attached to Table 2. When the reflectance spectrum is examined, it is clear that the anodization time and voltage cause a significant shift in the reflectance value of the sample. These changes in the reflectance data were observed due to the changes in the values in the bandgap which show a red-shift (< ~ 0.4 eV). The obtained eV was smaller than the bandgap of bulk ZnO (3.37 eV) and varying from 2.93 to 3.12 eV. For understanding the changes in the bandgap, many theoretical models, such as quantum confinement effect [62], color centers [63], free-exciton collision [64], surface states [65], and Burstein–Moss effect [66, 67] were developed. The observed declining trend in the bandgap is in good agreement with previous studies describing this behavior as a result of bulk defects that cause

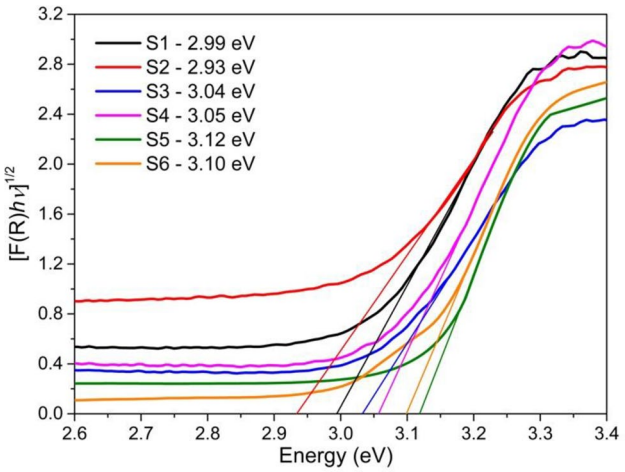

Fig. 6 Plots of Kubelka–Munk function versus the incident photon energy of ZnO samples

displacement of molecular orbitals at the conduction band edge and create deep traps in electronic energy [68, 69].

3.4 Photocatalytic activity

The photocatalytic mechanism of ZnO structures with different surface properties is shown in Fig. 7. When stimulated with light, the electrons in the valence band of ZnO are transferred to the conduction band. Thus, while gaps (h^+) are formed in the valence band, electrons pass into the (e^-) conduction band. When oxygen molecules (O_2) are excited by light, they are reduced with the O_2's emerging from ZnO and form superoxide radical anions ($\cdot O_2^-$). These O_2^- structures break down MB into green compounds such as carbon dioxide (CO_2) and water (H_2O). The reactions taking place during the decomposition of the MB under the UV–Vis light source can be listed as follows:

$$ZnO + h\upsilon \rightarrow ZnO\left(h^+ + e^-\right) \quad (1)$$

$$O_2 + e^- \rightarrow \cdot O_2^- \quad (2)$$

$$H_2O + h^+ \rightarrow \cdot OH + H^+ \quad (3)$$

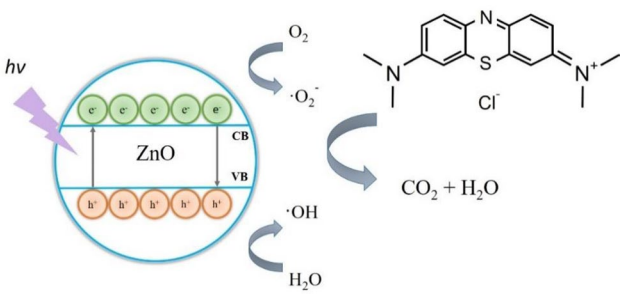

Fig. 7 The photocatalytic degradation mechanism of MB by ZnO nanostructures

$$h^+ + \cdot O_2^- + \cdot OH + MB \rightarrow CO_2 + H_2O \quad (4)$$

Photocatalytic performances of ZnO samples added into 10^{-5} M MB were evaluated by measuring the absorbance data of MB at certain time intervals. With the photocatalytic effect, photocatalysts break down MB aqueous solution over time and cause its color to be removed. Concentration data were obtained using the Lambert–Beer law from the absorbance values of the characteristic peak of MB at 664 nm for all samples. The rate constant of the photocatalytic degradation was calculated by using the integrated form of the first-order reaction rate (Eq. 5).

$$\ln \frac{C_0}{C} = kt. \quad (5)$$

In this equation, C_0 the initial concentration of MB, C it is the concentration of MB at any time t. The rate constant of degradation was shown as k. The photocatalytic degradation rate was calculated by using determined values. When the graph in Fig. 8a showing the change in MB concentration during 750 min is examined, it is seen that the sample that decreased the initial concentration of MB the most was the S4 sample. Adsorption capacity is an important parameter for improved photocatalytic performance. As seen in Fig. 8b, the results from adsorption in the dark medium show that all samples have good levels of adsorption ability. When all samples were examined, the S4 sample showed the best adsorption capacity of approximately 20%. These results

Table 2 Photocatalytic parameters of ZnO samples

Samples	Ref	S1	S2	S3	S4	S5	S6	[70]	[71]	[72]
Kinetic rate constant (k) (10^{-3} min^{-1})	0.43	1.82	2.24	2.29	2.89	2.09	1.84	0.2	1.5	2.4
R^2	0.993	0.999	0.996	0.994	0.999	0.999	0.994	–	–	–
Band gap (eV)	–	2.99	2.93	3.04	3.05	3.12	3.10	3.22	3.21	3.37

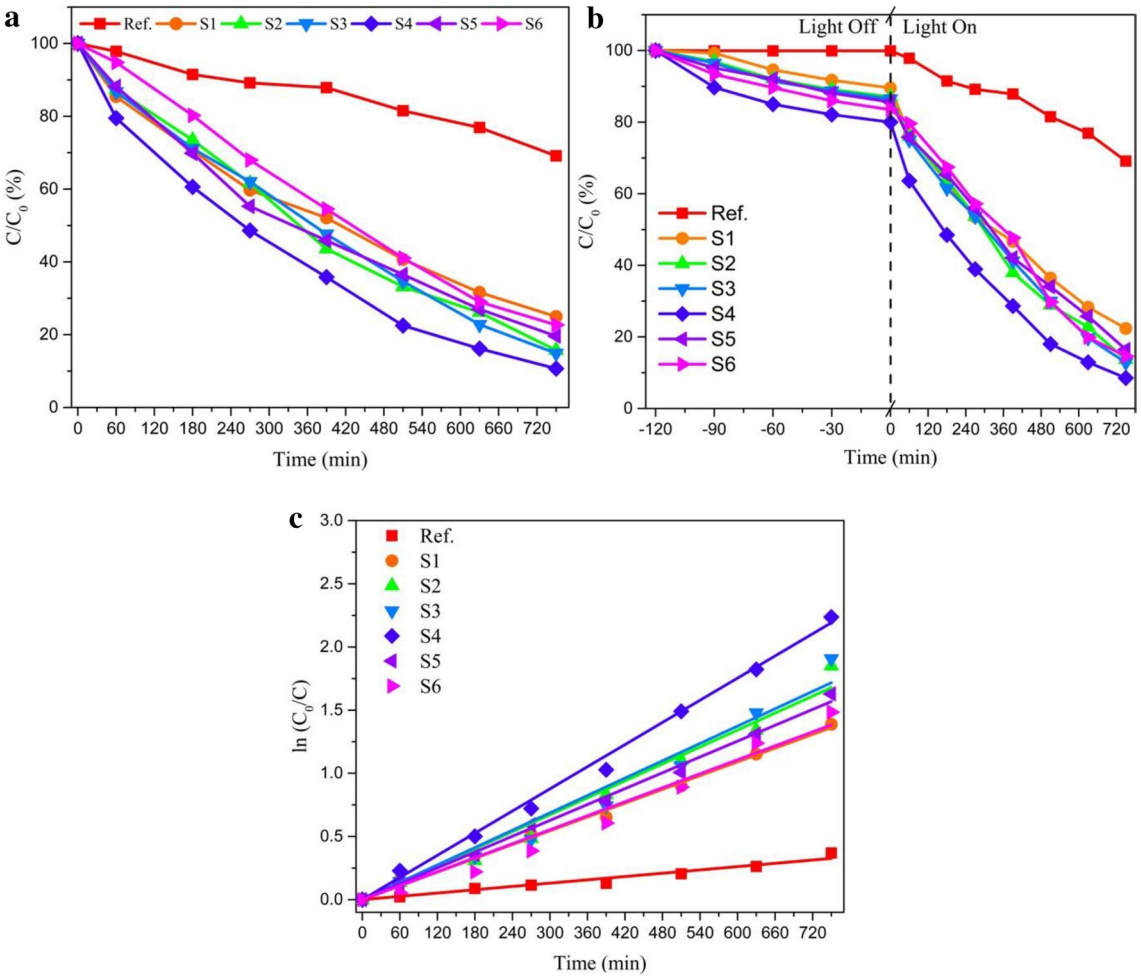

Fig. 8 Photocatalytic performances of ZnO samples for different anodization times

showed that the change in the anodizing parameters also affected the adsorption properties of the samples. When the total degradation values as a result of the adsorption and photo-degradation processes were examined, the S4 sample degraded the MB by 89.3%. The variation of the obtained $\ln(C_0/C)$ values over time was shown in Fig. 8c. When the graphics in Fig. 8 were examined, it was seen that the S4 sample has a maximum decomposition rate. The slope of the graph created in Fig. 8c gives the k value. The k values obtained showed that the photocatalytic degradation of MB correlated with surface morphology and oxide layer thickness. Photocatalytic parameters of all samples are given in Table 2. When the k values obtained in Table 2 were compared with the literature, it shows that the ZnO nanostructures produced within the scope of this study exhibit better photocatalytic performance.

The photodegradation curves of all samples at the wavelength range between 400 and 800 nm are given in Fig. 9. The degradation efficiencies of MB by different samples were calculated according to the initial absorbance value of 0.693 at 664 nm. These results were given in the bar chart in Fig. 10. As can be seen from Fig. 10, the S4 sample has the best photocatalytic performance with a degradation efficiency of 89.3% in 750 min where the arbitration sample was 30.9%. As another observation, the photocatalytic performance was affected by changing the anodization time, voltage, and electrolyte. As it is known, there are many factors that affect photocatalytic performance, such as morphology, surface area, crystallinity, phase composition, crystal orientation, and band gap [53]. Although the sample with the lowest bandgap is the S2 sample, the best photocatalyst is the S4 sample, which can be explained as a result of the synergistic effect of many factors such as surface area, oxide layer thickness and bandgap on the photocatalytic activity.

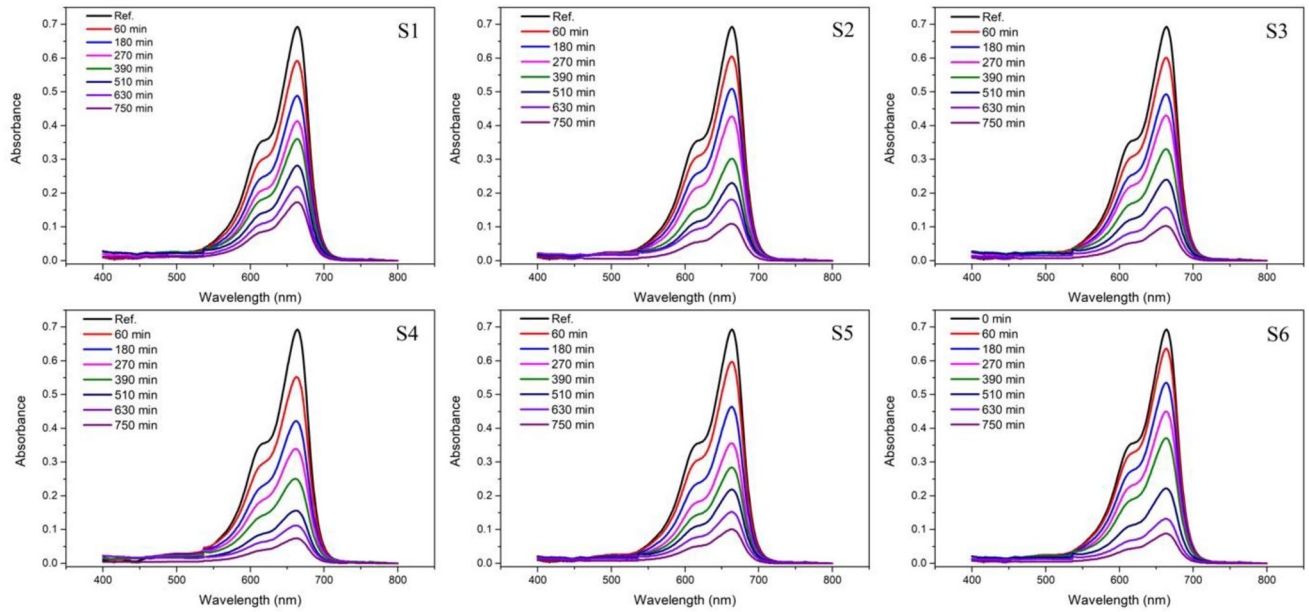

Fig. 9 Absorption spectra of MB for all samples anodized at different parameters

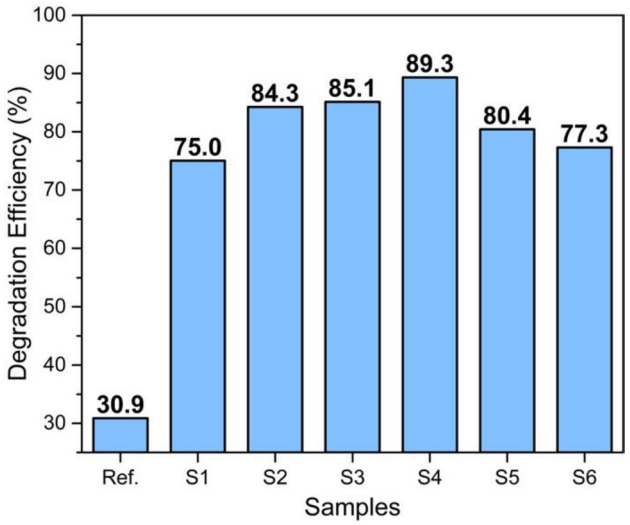

Fig. 10 Photocatalytic degradation efficiencies of MB by different samples under UV–Vis light irradiation

4 Conclusion

In summary, ZnO nanostructures with different morphologies were successfully prepared by varying anodizing parameters. ZnO growth conditions can be controlled with different solutions, voltages, and time which are important factors that affect the structure, morphology, and shape of ZnO nanostructures. The XRD results confirm that the ZnO coatings were formed on the Zn substrate. It can be seen that the ZnO nanostructures with different diameters and shapes are well distributed in different directions. The photocatalytic experiment indicated that the S4 sample anodized in 0.05 M $KHCO_3$ solution at 40 V for 60 min had superior photocatalytic performance in the degradation of methylene blue under UV–Vis irradiation with the degradation efficiency of 89.3%. These produced ZnO nanostructures have promising potential advantages in photocatalytic applications.

References

1. J. Xiao, Y. Xie, H. Cao, Organic pollutants removal in wastewater by heterogeneous photocatalytic ozonation. Chemosphere **121**, 1–17 (2015). https://doi.org/10.1016/j.chemosphere.2014.10.072
2. C.C. Wang, J.R. Li, X.L. Lv, Y.Q. Zhang, G. Guo, Photocatalytic organic pollutants degradation in metal-organic frameworks. Energy Environ. Sci. **7**, 2831–2867 (2014). https://doi.org/10.1039/c4ee01299b
3. I. Medina-Ramírez, J.L. Liu, A. Hernández-Ramírez, C. Romo-Bernal, G. PedrozaHerrera, J. Jáuregui-Rincón, M.A. Gracia-Pinilla, Synthesis, characterization, photocatalytic evaluation, and toxicity studies of TiO_2–Fe^{3+} nanocatalyst. J. Mater. Sci. **49**, 5309–5323 (2014). https://doi.org/10.1007/s10853-014-8234-z
4. R.R. Chen, Q.F. Ren, Y.X. Liu, Y. Ding, H.T. Zhu, C.Y. Xiong, W.C. Oh, Synthesis of g-C_3N_4/diatomite/MnO_2 composites and their enhanced photo-catalytic activity driven by visible light. J. Korean Ceram. Soc. **58**(5), 548–558 (2021)
5. K. Qi, B. Cheng, J. Yu, W. Ho, Review on the improvement of the photocatalytic and antibacterial activities of ZnO. J. Alloy. Compd. **727**, 792–820 (2017). https://doi.org/10.1016/j.jallcom.2017.08.142
6. M. Cao, F. Wang, J. Zhu, X. Zhang, Y. Qin, L. Wang, Mater. Lett. **192**, 1–4 (2017)

7. X.L. Wang, C.Y. Luan, Q. Shao, A. Pruna, C.W. Leung, R. Lortz, J.A. Zapien, A. Ruotolo, Effect of the magnetic order on the room-temperature band-gap of Mn-doped ZnO thin films. Appl. Phys. Lett. **102**, 102112 (2013)
8. V.K. Gupta, Suhas, Application of low-cost adsorbents for dye removal—a review. J. Environ. Manage. **90**, 2313–2342 (2009)
9. J. You, Y. Guo, R. Guo, X. Liu, A review of visible light-active photocatalysts for water disinfection: features and prospects. Chem. Eng. J. **373**, 624–641 (2019)
10. J. Singh, S. Palsaniya, R.K. Soni, Mesoporous dark brown TiO_2 spheres for pollutant removal and energy storage applications. Appl. Surf. Sci. **527**, 146796 (2020)
11. C. Xu, P. Ravi Anusuyadevi, C. Aymonier, R. Luque, S. Marre, Nanostructured materials for photocatalysis. Chem. Soc. Rev. **48**, 3868–3902 (2019)
12. D. Schultz, T. Yoon, Solar synthesis: prospects in visible light photocatalysis. Science **48**, 1239176 (2019)
13. H. Hu, Y. Lin, Y.H. Hu, Synthesis, structures and applications of single component core-shell structured TiO_2: a review. Chem. Eng. J. **375**, 122029 (2019)
14. A. Kumar, K. Kumar, V. Krishnan, Sunlight driven methanol oxidation by anisotropic plasmonic Au nanostructures supported on amorphous titania: influence of morphology on photocatalytic activity. Mater. Lett. **245**, 45–48 (2019)
15. A. Noypha, Y. Areerob, S. Chanthai, P. Nuengmatcha, Fe_2O_3-graphene anchored Ag nanocomposite catalyst for enhanced sonocatalytic degradation of methylene blue. J. Korean Ceram. Soc. **58**(3), 297–306 (2021)
16. M.R. Hoffmann, S.T. Martin, W. Choi, D.W. Bahnemann, Environmental applications of semiconductor photocatalysis. Chem. Rev. **95**, 69–96 (1995)
17. T.Q. Trang, T.B. Phan, N.D. Nam, V.T.H. Thu, In situ charge transfer at the Ag@ZnO photoelectrochemical interface toward the high photocatalytic performance of H_2 evolution and RhB degradation. ACS Appl. Mater. Interfaces **12**, 12195–12206 (2020)
18. A. Kumar, K.L. Reddy, S. Kumar, A. Kumar, V. Sharma, V. Krishnan, Rational design and development of lanthanide-doped NaYF4@CdS-Au-RGO as quaternary plasmonic photocatalysts for harnessing visible-near-infrared broadband spectrum. ACS Appl. Mater. Interfaces **10**, 15565–15581 (2018)
19. J. Singh, A.K. Manna, R.K. Soni, Bifunctional Au-TiO_2 thin films with enhanced photocatalytic activity and SERS based multiplexed detection of organic pollutant. J. Mater. Sci. Mater. El. **30**, 16478–16493 (2019)
20. J. Singh, R.K. Soni, Controlled synthesis of CuO decorated defect enriched ZnO nanoflakes for improved sunlight-induced photocatalytic degradation of organic pollutants. Appl. Surf. Sci. **521**, 146420 (2020)
21. K.L. Reddy, S. Kumar, A. Kumar, V. Krishnan, Wide spectrum photocatalytic activity in lanthanide-doped upconversion nanophosphors coated with porous TiO_2 and AgCu bimetallic nanoparticles. J. Hazard. Mater. **367**, 694–705 (2019)
22. K.M. Lee, C.W. Lai, K.S. Ngai, J.C. Juan, Recent developments of zinc oxide based photocatalyst in water treatment technology: a review. Water Res. **88**, 428–448 (2016)
23. S.P. Lonkar, V.V. Pillai, S.M. Alhassan, Facile and scalable production of heterostructured ZnS–ZnO/graphene nano-photocatalysts for environmental remediation. Sci. Rep. **8**, 13401–13414 (2018)
24. A. Kumar, V. Sharma, S. Kumar, A. Kumar, V. Krishnan, Towards utilization of full solar light spectrum using green plasmonic Au–TiOx photocatalyst at ambient conditions. Surf. Interface **11**, 98–106 (2018)
25. X. Wu, G. Lu, C. Li, G. Shi, Room-temperature fabrication of highly oriented ZnO nanoneedle arrays by anodization of zinc foil. Nanotechnology **17**, 4936 (2006). https://doi.org/10.1088/0957-4484/17/19/026
26. E.M.P. Steinmiller, K.-S. Choi, Anodic construction of lamellar structured ZnO films using basic media via interfacial surfactant templating. Langmuir **23**, 12710–12715 (2007). https://doi.org/10.1021/LA702066W
27. C.Y. Kuan, J.M. Chou, I.C. Leu, M.H. Hon, Formation and field emission property of single-crystalline Zn microtip arrays by anodization. Electrochem. Commun. **9**, 2093–2097 (2007). https://doi.org/10.1016/J.ELECOM.2007.06.004
28. S.S. Chang, S.O. Yoon, H.J. Park, A. Sakai, Luminescence properties of Zn nanowires prepared by electrochemical etching. Mater. Lett. **53**, 432–436 (2002). https://doi.org/10.1016/S0167-577X(01)00521-3
29. S.J. Kim, J. Choi, Self-assembled arrays of ZnO stripes by anodization. Electrochem. Commun. **10**, 175–179 (2008). https://doi.org/10.1016/J.ELECOM.2007.11.014
30. G.S. Huang, X.L. Wu, Y.C. Cheng, J.C. Shen, A.P. Huang, P.K. Chu, Fabrication and characterization of anodic ZnO nanoparticles. Appl. Phys. A **864**(86), 463–467 (2006). https://doi.org/10.1007/S00339-006-3778-7
31. A. Ramirez-Canon, D.O. Miles, P.J. Cameron, D. Mattia, Zinc oxide nanostructured films produced via anodization: a rational design approach. RSC Adv. **3**, 25323–25330 (2013). https://doi.org/10.1039/C3RA43886D
32. S.-Y. Kuo, F.-I. Lai, W.-C. Chen, C.-P. Cheng, H.-C. Kuo, S.-C. Wang, Ultraviolet lasing of sol–gel-derived zinc oxide polycrystalline films. Jpn. J. Appl. Phys. **45**, 3662 (2006). https://doi.org/10.1143/JJAP.45.3662
33. V. Musat, B. Teixeira, E. Fortunato, R.C.C. Monteiro, Effect of post-heat treatment on the electrical and optical properties of ZnO:Al thin films. Thin Solid Films **502**, 219–222 (2006). https://doi.org/10.1016/J.TSF.2005.07.278
34. M. Sahal, B. Hartiti, A. Ridah, M. Mollar, B. Marí, Structural, electrical and optical properties of ZnO thin films deposited by sol–gel method. Microelectronics J. **39**, 1425–1428 (2008). https://doi.org/10.1016/J.MEJO.2008.06.085
35. L. Lin, H. Liu, X. Zhang, ZnO-template synthesis of rattle-type catalysts with supported Pd nanoparticles encapsulated in hollow ZIF-8 for liquid hydrogenation. Chem. Eng. J. **328**, 124–132 (2017)
36. C. Bae, H. Yoo, S. Kim et al., Template-directed synthesis of oxide nanotubes: fabrication, characterization, and applications. Chem Mater **20**, 756–767 (2008)
37. A. Dauletbekova, A. Kozlovskyi, A. Akilbekov, A. Seitbayev, A. Alzhanova, Synthesis of ZnO nanocrystals in a-SiO_2/Si ion track templates. Surf. Coat. Technol. **355**, 11–15 (2018)
38. V. Gerbreders, M. Krasovska, E. Sledevskis, A. Gerbreders, I. Mihailova, E. Tamanis, A. Ogurcovs, Hydrothermal synthesis of ZnO nanostructures with controllable morphology change. CrystEngComm **22**(8), 1346–1358 (2020)
39. M. Zare, K. Namratha, M.S. Thakur, K. Byrappa, Biocompatibility assessment and photocatalytic activity of bio-hydrothermal synthesis of ZnO nanoparticles by Thymus vulgaris leaf extract. Mater. Res. Bull. **109**, 49–59 (2019)
40. E. Muchuweni, T.S. Sathiaraj, H. Nyakotyo, Hydrothermal synthesis of ZnO nanowires on rf sputtered Ga and Al co-doped ZnO thin films for solar cell application. J. Alloy. Compd. **721**, 45–54 (2017)
41. L. Zhu, Y. Li, W. Zeng, Hydrothermal synthesis of hierarchical flower-like ZnO nanostructure and its enhanced ethanol gas-sensing properties. Appl. Surf. Sci. **427**, 281–287 (2018)
42. T. Sansenya, N. Masri, T. Chankhanittha, T. Senasu, J. Piriyanon, S. Mukdasai, S. Nanan, Hydrothermal synthesis of ZnO photocatalyst for detoxification of anionic azo dyes and antibiotic. J. Phys. Chem. Solids **160**, 110353 (2021)

43. C. Feng, F. Wen, Z. Ying, L. Li, X. Zheng, P. Zheng, G. Wang, Polypeptide-assisted hydrothermal synthesis of ZnO for room temperature NO_2 gas sensor under UV illumination. Chem. Phys. Lett. **754**, 137745 (2020)
44. X. Shao, W. Xin, X. Yin, Hydrothermal synthesis of ZnO quantum dot/KNb_3O_8 nanosheet photocatalysts for reducing carbon dioxide to methanol. Beilstein J. Nanotechnol. **8**(1), 2264–2270 (2017)
45. Y. Wei, X. Wang, G. Yi, L. Zhou, J. Cao, G. Sun, Z. Zhang, Hydrothermal synthesis of Ag modified ZnO nanorods and their enhanced ethanol-sensing properties. Mater. Sci. Semicond. Process. **75**, 327–333 (2018)
46. E. Muchuweni, T.S. Sathiaraj, H. Nyakotyo, Effect of annealing on the microstructural, optical and electrical properties of ZnO nanowires by hydrothermal synthesis for transparent electrode fabrication. Mater. Sci. Eng., B **227**, 68–73 (2018)
47. H.W. Kim, Y.J. Kwon, A. Mirzaei, S.Y. Kang, M.S. Choi, J.H. Bang, S.S. Kim, Synthesis of zinc oxide semiconductors-graphene nanocomposites by microwave irradiation for application to gas sensors. Sens. Actuators B Chem. **249**, 590–601 (2017)
48. M. Darvishi, F. Jamali-Paghaleh, M. Jamali-Paghaleh, J. Seyed-Yazdi, Facile synthesis of ZnO/rGO hybrid by microwave irradiation method with improved photoactivity. Surf. Interfaces **9**, 167–172 (2017)
49. A. Ravanbakhsh, F. Rashchi, M. HeydarzadehSohi, R. Khayyam Nekouei, M. MortazaviSamarin, Synthesis and characterization of porous zinc oxide nano-flakes film in alkaline media. J. Ultrafine Grained Nanostruct. Mater. **51**(1), 32–42 (2018)
50. L. Tn, P. Tt, N. Qm, V. Th, Electrochemical synthesis of ZnO nanorods/nanotubes/nanopencils on transparent aluminium-doped zinc oxide thin films for photocatalytic applications. J. Nanosci. Nanotechnol. **15**, 6568–6575 (2015). https://doi.org/10.1166/JNN.2015.10502
51. T.G. Venkatesha, Y.A. Nayaka, R. Viswanatha, C.C. Vidyasagar, B.K. Chethana, Electrochemical synthesis and photocatalytic behavior of flower shaped ZnO microstructures. Powder Technol **225**, 232–238 (2012). https://doi.org/10.1016/J.POWTEC.2012.04.021
52. S. Anandan, T. Narasinga Rao, M. Sathish et al., Superhydrophilic graphene-loaded TiO_2 thin film for self-cleaning applications. ACS Appl Mater Interfaces **5**, 207–212 (2013). https://doi.org/10.1021/am302557z
53. T. Dikici, S. Yildirim, M. Yurddaskal et al., A comparative study on the photocatalytic activities of microporous and nanoporous TiO_2 layers prepared by electrochemical anodization. Surf Coat Technol **263**, 1–7 (2015)
54. M. Yurddaşkal, U. Kartal, E.C. Doluel, Titanyum Dioksit/İndirgenmiş Grafen Oksit Kompozitlerin Üretimi ve Fotokatalitik Özelliklerinin İncelenmesi. J Polytech **0900**, 249–255 (2019). https://doi.org/10.2339/politeknik.537900
55. S.D. Ponja, S. Sathasivam, I.P. Parkin, C.J. Carmalt, Highly conductive and transparent gallium doped zinc oxide thin films via chemical vapor deposition. Sci. Rep. **10**(1), 1–7 (2020)
56. E. Ersöz, Y.O. Altintas, Green synthesis and characterization of Ag-doped ZnO nanofibers for photodegradation of MB, RhB and MO dye molecules. J. Korean Ceram. Soc. 1–16 (2022).
57. A. Kumar, D.P. Sammaiah, Influence of process parameters on mechanical and metallurgical properties of zinc coating on mild steel during mechanical process. Current research topics in poweer, Nuclear and Fuel Energy, SP-CRTPNFE (2017).
58. K. Mika, R.P. Socha, P. Nyga, E. Wiercigroch, K. Małek, M. Jarosz, L. Zaraska, Electrochemical synthesis and characterization of dark nanoporous zinc oxide films. Electrochim. Acta **305**, 349–359 (2019)
59. D. Stock, S. Dongmo, D. Damtew, M. Stumpp, A. Konovalova, D. Henkensmeier, D. Schröder, Design strategy for zinc anodes with enhanced utilization and retention: electrodeposited zinc oxide on carbon mesh protected by ionomeric layers. ACS Appl. Energy Mater. **1**(10), 5579–5588 (2018)
60. P. Basnet, D. Samanta, T.I. Chanu, J. Mukherjee, S. Chatterjee, Assessment of synthesis approaches for tuning the photocatalytic property of ZnO nanoparticles. SN Appl. Sci. **1**(6), 1–13 (2019)
61. M.A. Nazir, T. Mahmood, N. Akhtar, K. Hussain, W.S. Khan, M.A. Waqar, J. Raza, Effect of high pressure on structural, electrical, and optical properties of graphene-like zinc oxide (g-ZnO) structure. Mater. Sci. Semicond. Process. **142**, 106465 (2022)
62. Y. Lv, W. Xiao, W. Li, J. Xue, J. Ding, Controllable synthesis of ZnO nanoparticles with high intensity visible photoemission and investigation of its mechanism. Nanotechnology **24**(17), 175702 (2013)
63. G.G. Qin, H.Z. Song, B.R. Zhang, J. Lin, J.Q. Duan, G.Q. Yao, Experimental evidence for luminescence from silicon oxide layers in oxidized porous silicon. Phys. Rev. B **54**(4), 2548 (1996)
64. Y.D. Glinka, S.H. Lin, L.P. Hwang, Y.T. Chen, N.H. Tolk, Size effect in self-trapped exciton photoluminescence from SiO_2-based nanoscale materials. Phys. Rev. B **64**(8), 085421 (2001)
65. C.W. Chen, K.H. Chen, C.H. Shen, A. Ganguly, L.C. Chen, J.J. Wu, W.F. Pong, Anomalous blueshift in emission spectra of ZnO nanorods with sizes beyond quantum confinement regime. Appl. Phys. Lett. **88**(24), 241905 (2006)
66. Y.H. Yang, X.Y. Chen, Y. Feng, G.W. Yang, Physical mechanism of blue-shift of UV luminescence of a single pencil-like ZnO nanowire. Nano Lett. **7**(12), 3879–3883 (2007)
67. A.S. Al-Asadi, L.A. Henley, S. Ghosh, A. Quetz, I. Dubenko, N. Pradhan, N. Ali, Fabrication and characterization of ultraviolet photosensors from ZnO nanowires prepared using chemical bath deposition method. J. Appl. Phys. **119**(8), 084306 (2016)
68. H. Lin, C.P. Huang, W. Li, C. Ni, S.I. Shah, Y.H. Tseng, Size dependency of nanocrystalline TiO_2 on its optical property and photocatalytic reactivity exemplified by 2-chlorophenol. Appl. Catal. B **68**(1–2), 1–11 (2006)
69. L. Brus, Electronic wave functions in semiconductor clusters: experiment and theory. J. Phys. Chem. **90**(12), 2555–2560 (1986)
70. W. Vallejo, A. Cantillo, C. Díaz-Uribe, Methylene blue photodegradation under visible irradiation on Ag-Doped ZnO thin films. Int. J. Photoenergy **2020**, 1627498 (2020)
71. R. Saravanan, E. Sacari, F. Gracia, M.M. Khan, E. Mosquera, V.K. Gupta, Conducting PANI stimulated ZnO system for visible light photocatalytic degradation of coloured dyes. J. Mol. Liq. **221**, 1029–1033 (2016)
72. N.R. Khalid, A. Hammad, M.B. Tahir, M. Rafique, T. Iqbal, G. Nabi, M.K. Hussain, Enhanced photocatalytic activity of Al and Fe co-doped ZnO nanorods for methylene blue degradation. Ceram. Int. **45**(17), 21430–21435 (2019)